THE JOURNAL OF PHYSICAL CHEMISTRY B
A JOURNAL OF THE AMERICAN CHEMICAL SOCIETY

pubs.acs.org/JPCB

Article

Probing the Structural Topology and Dynamic Properties of gp28 Using Continuous Wave Electron Paramagnetic Resonance Spectroscopy

Rasal H. Khan, Nancy C. Rotich, Andrew Morris, Tanbir Ahammad, Binaya Baral, Indra D. Sahu, and Gary A. Lorigan*

Cite This: J. Phys. Chem. B 2023, 127, 9236–9247

Read Online

ACCESS | Metrics & More | Article Recommendations | Supporting Information

ABSTRACT: Lysis of Gram-negative bacteria by dsDNA phages is accomplished through either the canonical holin-endolysin pathway or the pinholin-SAR endolysin pathway. During lysis, the outer membrane (OM) is disrupted, typically by two-component spanins or unimolecular spanins. However, in the absence of spanins, phages use alternative proteins called Disruptin to disrupt the OM. The Disruptin family includes the cationic antimicrobial peptide gp28, which is found in the virulent podophage φKT. In this study, EPR spectroscopy was used to analyze the dynamics and topology of gp28 incorporated into a lipid bilayer, revealing differences in mobility, depth parameter, and membrane interaction among different segments and residues of the protein. Our results indicate that multiple points of helix 2 and helix 3 interact with the phospholipid membrane, while others are solvent-exposed, suggesting that gp28 is a surface-bound peptide. The CW-EPR power saturation data and helical wheel analysis confirmed the amphipathic-helical structure of gp28. Additionally, course-grain molecular dynamics simulations were further used to develop the structural model of the gp28 peptide associated with the lipid bilayers. Based on the data obtained in this study, we propose a structural topology model for gp28 with respect to the membrane. This work provides important insights into the structural and dynamic properties of gp28 incorporated into a lipid bilayer environment.

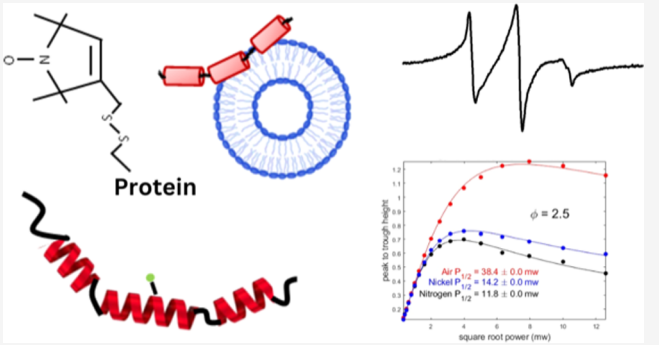

INTRODUCTION

Phage lysis is one of the most common cell fates on this planet except for cell division.[1] dsDNA phages in Gram-negative hosts remain the most utilized system for studying the molecular details of phage lysis.[2] The phage lysis of Gram-negative hosts follows either the canonical holin-endolysin pathway or the pinholin signal anchor release (SAR) endolysin pathway.[3] Both pathways follow a three-step lysis process, and each step involves a different class of lysis proteins: holins, endolysins and spanins.[2,4,5] Among each functional class of lysis proteins, there are two distinct subclasses with different membrane topologies.[2] This lytic process begins with holin creating a hole in the inner cytoplasmic membrane (IM), followed by endolysin degrading the peptidoglycan (PG) and spanin disrupting the outer membrane (OM).[6−9] Holins can be either canonical holins or pinholins.[2] Canonical holins form micron-scale holes that enable endolysin to escape from the cytoplasm into the periplasm and degrade PG.[2,3] Pinholins are associated with membrane-tethered SAR-endolysin. At an allele-specific time pinholins form smaller pinholes (~10^3 nm scale) and SAR-endolysin is released into the periplasm to degrade the PG.[2,4] Disruption of the OM, the last step of lysis, also offers two different molecular solutions in the form of two-component spanins (o-spanin and i-spanin) and the unimolecular spanin (u-spanin).[2,10,11] However, according to a recent bioinformatic study of 677 genomes of Gram-negative bacteria-infecting phages, about 15% of these phages lack spanins but are still able to lyse the bacterial cell.[12] The findings indicate that some phages disrupt the OM differently and may involve different proteins. Termed Disruptins, this new class of proteins are discussed in terms of a new model for the coordination of phage lysis.[12] gp28 is designated as the founding member of the Disruptin family.[12] gp28 is a small (56 amino acids long) cationic antimicrobial peptide (CAMP), consisting of three predicted alpha helices, with a net charge of +7 at pH 7. The peptide is produced by φKT, a podophage of

Received: May 31, 2023
Revised: September 22, 2023
Published: October 19, 2023

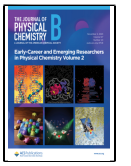

https://doi.org/10.1021/acs.jpcb.3c03679
J. Phys. Chem. B 2023, 127, 9236−9247

E. coli where it complements lambda lysis defects caused by spanin.[12,13] To protect against microbes, many organisms produce CAMPs, which generally act by disrupting or perforating bacterial membranes. Antimicrobial activity of CAMPs is influenced by factors such as amphipathicity, net charge, hydrophobicity, cationic residue position, and conformation. Because of their amphipathic secondary structure, their overall positive charge allows them to strongly interact with highly negatively charged bacterial membranes.[14] The Ry Young group reported gp28 as a CAMP and conducted biomolecular and functional experiments, as well as computational studies to predict the hydrophobic and hydrophilic regions of the three helices.[12] However, the motional dynamics as well as relative orientations and interactions of helices with membranes have not been extensively investigated. In order to investigate the structural model proposed by the Ry young group, we synthesized gp28 and probed its structural and dynamic properties in a reconstituted model membrane via Electron Paramagnetic Resonance (EPR) spectroscopy. Additionally, we developed a structural topology model for gp28 in the presence of a lipid bilayer membrane combining the CW-EPR data and the insights obtained from the results of Course-grain molecular dynamics simulation.

The structural topology of proteins and their dynamic properties are both important factors to understand their function and stability.[15−19] In this study, we aim to understand the structural topology and dynamic properties of gp28 in its nativelike environment using EPR spectroscopic techniques. With EPR spectroscopy, we can probe the structure and dynamics of spin-labeled proteins with a high degree of sensitivity in conditions mimicking a cell membrane.[7,8,15,20−30]

Fmoc solid-phase peptide synthesis (Fmoc-SPPS) was used to synthesize spin-labeled peptides with Cys mutation at different positions to build a library of EPR active gp28 constructs [Figure 1A,B].[31] A nitroxide spin-label, MTSL (*S*-

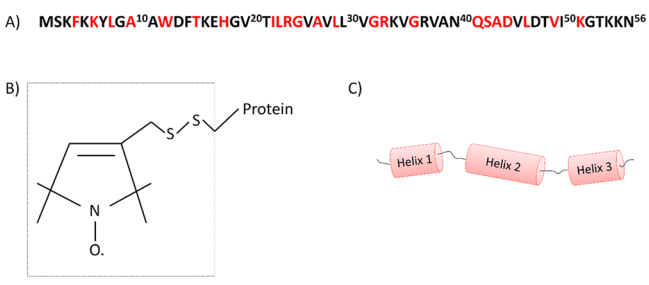

Figure 1. (A) Illustration of the primary sequence of wild type (WT) gp28 with the spin-label positions highlighted in red. (B) The protein is linked to the R1 spin-label through a disulfide bond on its side-chain. (C) The secondary structure of gp28 is illustrated based on a previous publication: α helix 1 (amino acid 3−10), α helix 2 (amino acid 20−38), and α helix 3 (amino acid: 42−51).[12]

(1-oxyl-2,2,5,5-tetramethyl-2,5-dihydro-1*H*-pyrrol-3-yl)-methylethanesulfonothioate), was attached site-specifically to Cys using site-directed spin-labeling (SDSL).[32] Based on our CW-EPR spectroscopic line shape analysis and EPR power saturation data, a tentative structural topology model of the gp28 peptide in a membrane is proposed, where multiple points of helix 2 and helix 3 show obvious interaction with the lipid bilayers and others are solvent-exposed. The data indicate that gp28 is a surface-bound peptide. However, the data obtained for helix 1 did not show any conclusive interaction with the lipid bilayer indicating that either helix 1 is fully solvent-exposed or may have electrostatic interaction with the phosphate headgroup due to the presence of opposite charge on it.

EXPERIMENTAL METHODS

Peptide Synthesis and Purification. All peptides were synthesized (0.1 mmol) using optimized Fmoc SPPS.[7−9] The peptide synthesis was carried out on an automated CEM Liberty Blue peptide synthesizer equipped with a Discovery Bio microwave system. In each synthesis, asparagine-preloaded TGA resin was used in a dimethylformamide (DMF) solvent system. To remove the Fmoc-protecting group from the protected amino acids before each coupling cycle, piperidine in DMF (20% (v/v)) was used as a deprotector. Each coupling cycle started with the addition of 0.2 M amino acids to the reaction vessel in combination with 15.6% (v/v) *N*,*N*′-diisopropylcarbodiimide (DIC) and 14.2% (w/v) oxyma as activator and activator base, respectively. Upon successful synthesis, the cleavage reaction (with TFA, TIPS, EDDT, and water) was run for at least 3 h under optimized cocktail conditions followed by filtration, N_2 (g) evaporation, and ether precipitation. To obtain a fluffy and easy-to-solubilize crude powder peptide, peptide pellets were then washed three more times with ice-cold ether, followed by centrifugation. Purification of the crude peptide was then performed using reversed-phase HPLC using a GE HPLC system and a C4 (10 μM) preparative column (Vydac 214TP, 250 × 22 mm).[33−35] We used a two-solvent gradient system, with the polar solvent being water and the nonpolar solvent being acetonitrile with 10% water. Both solvents were acidified with TFA (0.1%). Lyophilized pure peptide was dissolved in dimethyl sulfoxide (DMSO) with a 5-fold excess of MTSL (1:5 molar ratio) and stirred overnight at room temperature in a dark environment to attach the spin-label. The spin-labeled (SL) peptide was lyophilized again and purified with a C4 semipreparative column (Vydac 214TP, 250 × 10 mm), using the same solvent and gradient system to remove free MTSL and further purify the peptide sample.[7−9,33−35] The purity of the target peptide was confirmed by using ESI-MS after each purification. Spin-labeling efficiency was calculated to be 85−90% by using a CW-EPR calibration curve.[33]

Incorporation of Peptide into Proteoliposomes. In order to simulate a membrane environment, spin-labeled peptides were incorporated into POPC (1-palmitoyl-2-oleoyl-*sn*-glycero-3-phosphocholine)/POPG (1-palmitoyl-2-oleoyl-*sn*-glycero-3-phospho-(1′-rac-glycerol)) (3:1, mol:mol) proteoliposomes.[7,9,33] The pure spin-labeled peptide was dissolved in 2,2,2-trifluoroethanol (TFE) and mixed with predissolved POPC/POPG lipid solution in a pear-shaped flask. To remove any residual organic solvent, N_2(g) purging was used to gently evaporate the organic solvent inside a pear-shaped flask, followed by overnight vacuum desiccation. To rehydrate the thin film, 10 mM HEPES (4-(2-hydroxyethyl)-1-piperazineethanesulfonic acid) buffer (pH 7.0) was used to obtain a final concentration of 200 mM lipid and 200 μM peptide. To obtain uniform liposomes, freeze−thaw−vortex cycles were performed at least three times. Afterward, glycerol (10% of the final volume) was added, and the mixture was mixed thoroughly. Dynamic light scattering (DLS) spectroscopy (ZEETASIZER NANO Series; Malvern Instruments) was used to confirm the sample homogeneity and uniformity of

https://doi.org/10.1021/acs.jpcb.3c03679
J. Phys. Chem. B 2023, 127, 9236−9247

proteoliposome size in a disposable 40 μL microcuvette at 25 °C.

Circular Dichroism Spectroscopy. The circular dichroism (CD) data were obtained using an Aviv Circular Dichroism Spectrometer (Model 435) in a quartz cuvette with a path length of 1.0 mm. CD spectra were obtained both in solution form by dissolving the pure peptide sample in TFE and in liposomes dispersed in excess HEPES buffer. At 25 °C, three scans per sample were collected from 200 to 260 nm with a 1 nm bandwidth.

CW-EPR Spectroscopy. CW-EPR spectra were collected at the X-band (~9.34 GHz) using a Bruker EMX spectrometer equipped with an ER041xG microwave bridge and an ER4119-HS cavity at Miami University Ohio's Advanced EPR Laboratory. The spectra were acquired at room temperature by signal-averaging 10 scans with 3305 G central field, 150 G sweep width, 42 s field sweep, 100 kHz modulation frequency, 1 G modulation amplitude, and 10 mW microwave power.[15,30,36]

Spin-Label Mobility Analysis. To determine the side-chain mobility, the inverse line width (δ^{-1}) of the first-derivative central resonance line ($m_I = 0$) was calculated. Using eq 1, the mobility parameter (δ^{-1}) was normalized to the "scaled mobility" factor (M_s).

$$M_s = \frac{\delta^{-1} - \delta_i^{-1}}{\delta_m^{-1} - \delta_i^{-1}} \tag{1}$$

where δ_i and δ_m are the central line widths for the most immobilized and the most mobile side chains, respectively. In order to calculate the mean scaled mobility ($\bar{M}_s$), all studied SL residues were averaged. The rotational correlation time (τ) was calculated using eq 2 to further investigate the dynamic properties.[20,21,37−39]

$$\tau = K\delta\left[\sqrt{\left(\frac{h_0}{h_{-1}} - 1\right)} - 1\right] \tag{2}$$

Here, $K = 6.5 \times 10^{-10}$ s and δ is the width of the center line of CW EPR spectra. The height of the center line and high field line are h_0 and h_{-1}, respectively.[38,39]

CW-EPR Power Saturation Experiments. A Bruker EMX X-band spectrometer coupled with an ER041XG microwave bridge and an ER4123D CW-resonator (Bruker BioSpin) was used for the CW-EPR power saturation experiments. Experimental setups were optimized as previously published.[7,8,27,37−39] The EPR data were collected at a modulation amplitude of 1 G, modulation frequency of 100 kHz, 42s field sweep, and a sweep width 90 G. Microwave incident power was attenuated in increments of 2 dB each from 159 to 0.06 mW. In a TPX capillary tube with a total volume of 3−4 μL and a concentration of 150 μM, samples were loaded for the power saturation experiments.[40−43] Three to five scans were taken at each microwave power. There were three equilibrium conditions for each spin-labeled site, and the experiments were repeated three times for each condition. First, samples were equilibrated with a lipid-soluble paramagnetic relaxant (21% oxygen), followed by equilibration with nitrogen gas (as a control), and finally with a water-soluble paramagnetic relaxant (2 mM NiEDDA) with continuous nitrogen purging.[7,8,43] NiEDDA was synthesized in accordance with published procedures.[23,43] Before starting nitrogen or NiEDDA data acquisition, the samples were purged with nitrogen gas for at least 1 h at a rate of 10 mL per minute. During all measurements, the resonator was connected to a gas supply (air as a source of 21% oxygen or nitrogen gas) at room temperature. Peak-to-peak amplitudes (A) of the first derivative ($m_I = 0$) resonance lines were plotted against the square root of incident microwave power. The data points were then fitted according to eq 3.[23,42]

$$A = I\sqrt{P}\left[1 + \frac{(2^{1/\varepsilon} - 1)P}{P_{1/2}}\right]^{-\varepsilon} \tag{3}$$

Here, I is a scaling factor, $P_{1/2}$ represents the power where the first derivative amplitude is reduced to half of its unsaturated value, and ε is a measure of the homogeneity of saturation of the resonance line. For the homogeneous and inhomogeneous saturation limits, $\varepsilon = 1.5$ and $\varepsilon = 0.5$, respectively. Using eq 4, the corresponding depth parameters were calculated.[23]

$$\Phi = \ln\left[\frac{\Delta P_{1/2}(O_2)}{\Delta P_{1/2}(\text{NiEDDA})}\right] \tag{4}$$

Here, $\Delta P_{1/2}$(NiEDDA) is the difference in the $P_{1/2}$ values for NiEDDA and nitrogen equilibriums and $\Delta P_{1/2}(O_2)$ is the difference in the $P_{1/2}$ values for oxygen and nitrogen equilibriums.

Molecular Dynamics Simulations of gp28. *Model Generation.* A model membrane bilayer was created using the bilayer builder module of martini maker in CHARMM-GUI with the martini22p force field.[44−47] It consisted of 150 molecules of POPC and 50 molecules of POPG per leaflet sandwiched between 22.5 nm of water. Ten different soluble models of gp28 were generated for input by manually building the sequence in UCSF Chimera.[48] Residues 4−10, 21−39, and 45−49 were assigned ideal alpha helical geometry with Φ of −57° and Ψ of −47° based on previously published prediction of secondary structure and circular dichroism data.[12] All other residues were assigned random backbone angles to sample a wide variety of relative orientations, with side chains built from the Dunbrack rotamer library.[49] Clashes generated this way were adjusted by 1,000 steps of steepest descent followed by 100 steps of conjugate gradient minimization of the all-atom model within Chimera. The resulting model was then converted into input for coarse-grained (CG) simulation using CHARMM-GUI martini maker solution builder and the Martini22p force field.[44,47] The resulting CG models for both the membrane and the peptide in solution had Na^+ and Cl^- present to produce a charge neutral system with 150 mM ions.

Molecular Dynamics Parameters. The Verlet scheme was utilized by searching for neighboring beads every 20 steps with a 0.005 buffer tolerance in a grid. Electrostatic interactions were calculated using the reaction-field scheme and a relative dielectric constant of 2.5, while van der Waals interactions were calculated with a cutoff scheme and a potential-shift-Verlet modifier. The cutoff distance for both interactions was 1.1 Å. Temperature was coupled separately for lipid, aqueous, and protein groups (when present in the system) by using velocity rescaling with a time constant of 1 ps and reference temperature of 303.15 K for all coupling groups. For the membrane and combined membrane-protein systems, the Berendsen barostat was utilized during the equilibration phase with a time constant of 5 ps, while Parrinello−Rahman was used during production with a time constant of 12 ps time constant. In both cases, pressure coupling was semi-isotropic

https://doi.org/10.1021/acs.jpcb.3c03679
J. Phys. Chem. B 2023, 127, 9236−9247

with a compressibility of 0.0003 bar^{-1} and a reference pressure of 1 bar along both the XY plane and z dimension.[50] All simulations were performed on the Redhawk cluster at Miami University.

The POPC/POPG CG membrane system was then minimized and equilibrated. Minimization was performed with 10,000 steps of steepest descent with flexible water at 1 fs time steps. Equilibration was performed in 5 steps: first, 500,000 steps with a 2 fs step time, then 200,000 steps of 5 fs, 100,000 steps of 10 fs, 50,000 steps of 15 fs, and then 50,000 steps of 20 fs. A positional restraint on lipid headgroup motion in the z direction was implemented during these equilibration steps, with a decreasing force constant of 200, 100, 50, 20 and then 10 in each step, respectively. This was followed by a 1,000,000 steps production phase with 20 fs time steps (20 ns total).

For the CG models of soluble gp28, 6,000 steps of steepest descent minimization with 20 fs time steps were performed. Equilibration was 500,000 steps with a 20 fs time step and positional restraints on the peptide with a force constant of 4,000. The production phase for each was 5,000,000 steps with 20 fs time steps (100 ns total) to allow sampling of different conformations of the flexible loops.

The final frame from production for the POPC/POPG membrane was combined with the final frame coordinates from production runs of each of the soluble GP28 peptides, as well as a neutralizing number of ions for the peptide. Peptide molecules were translated in VMD so that their starting position was a minimum of 7 Å from the closest lipid bead.[51] Minimization, equilibration, and production were performed with the same parameters as for the membrane-only simulation, except with 100,000 minimization steps. The production trajectory was run for 50,000,000 steps with 20 fs time steps (1 μs total) with frames written at 100 ps intervals. For 2 of 10 runs, this was extended to 150,000,000 steps when stable adsorption had not occurred during that time frame.

Simulation Data Interpretation. Depth within the membrane for each residue was determined as the difference between the mean position along the z axis of all phosphate beads within 7 Å of any peptide bead in that frame and the z position of a given peptide backbone bead. This was calculated for each frame in which the peptide was in a stable position on the membrane surface and then averaged over those frames for each residue using a custom script in VMD.

Contact mapping for each residue was done through a custom script in VMD. In each frame, each positive or partial positive bead in side-chains was surveyed for phosphate beads within a 4 Å cutoff radius, while negative and partial negative side chains were monitored for choline beads within the 4 Å cutoff radius. The number inside this radius for each frame was recorded and built into a time course.

RESULTS

The full length gp28 peptide and spin-labeled constructs were synthesized by using solid-phase peptide synthesis. Mass spectrometry confirmed that the synthesis was optimized to match the predicted molecular weights (Supplementary Figure S1). The MIC (minimum inhibitory concentration) value of gp28 after synthesis was tested, as in the literature it had been previously shown to be bactericidal.[12] Similar MIC values were observed for the wild type (WT) and spin-labeled gp28 construct (Supplementary Figure S2). However, MIC studies on additional spin-labeled gp28 constructs would be helpful to understand the antimicrobial activity of gp28 peptide, and the functional effects of individual Cys mutations cannot be ruled out. In this study, we aim to investigate the structural and dynamic properties of gp28 by analyzing the CW-EPR spectra and power saturation data of 23 spin-labeled constructs of the peptide incorporated into POPC/POPG proteoliposomes. To confirm the homogeneity of the proteoliposomes, DLS data were obtained after the incorporation of the peptides. Representative DLS data are shown in Figure 2 for gp28

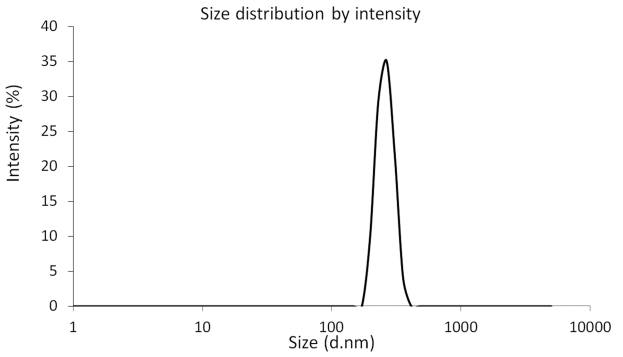

Figure 2. DLS data of gp28 R33R1 incorporated into POPC/POPG vesicles. Signal intensity is plotted as a log function of the particle diameter.

R33R1 incorporated into proteoliposomes, which confirms that the samples are homogeneous. Circular dichroism (CD) spectroscopy was used to evaluate proper folding and α-helical secondary structure of gp28 peptide samples. CD spectra were obtained for gp28 WT and spin-labeled gp28 constructs in vesicles dispersed into buffer solution to demonstrate that the spin-label incorporation has no significant effect on the secondary structure of the protein. Representative CD data are shown in Figure 3. Both CD spectra exhibit two minima at around 222 and 208 nm, indicating that the gp28 peptide has α-helical secondary structural components.[52] Based on the CD data, it was confirmed that nitroxide spin-labeling did not have

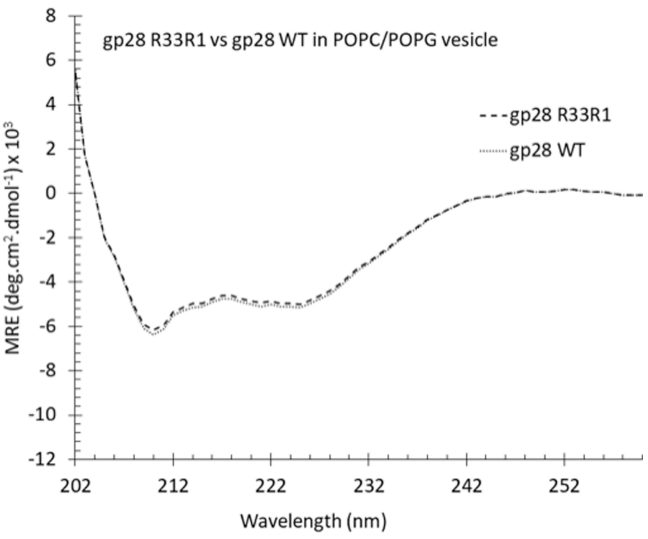

Figure 3. Circular dichroism spectra for gp28 wild type (WT) and spin-labeled gp28 R33R1 into POPC/POPG proteoliposomes. CD spectra were signal averaged for five scans. Mean residue molar ellipticity (MRE) is plotted against the incident radiation wavelength.

https://doi.org/10.1021/acs.jpcb.3c03679
J. Phys. Chem. B 2023, 127, 9236−9247

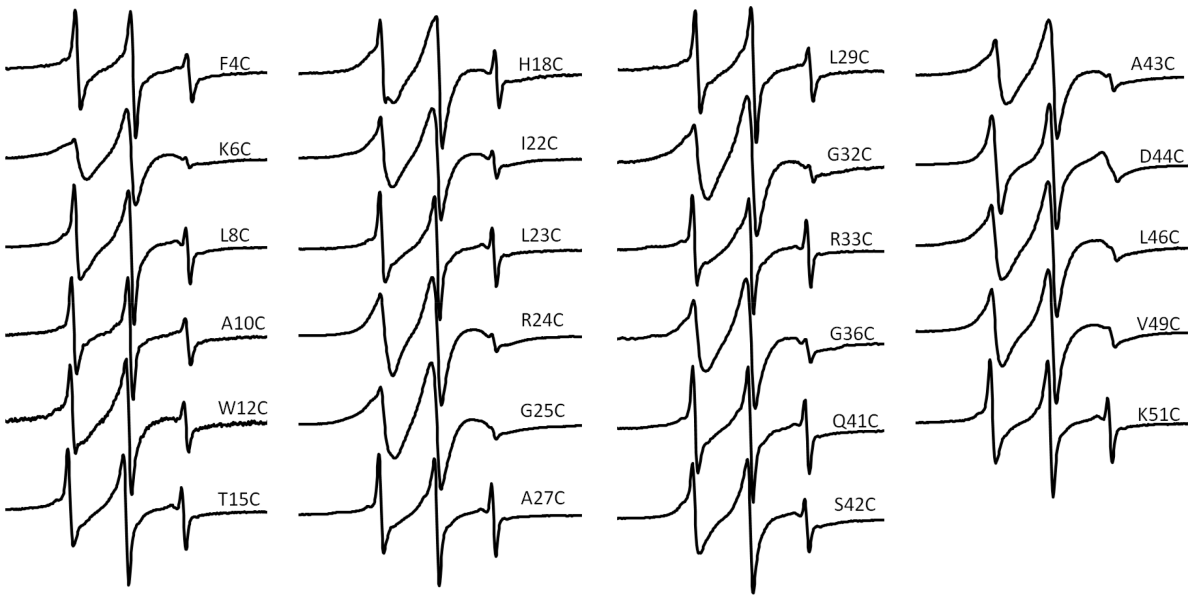

Figure 4. Representative CW-EPR spectra of spin-labeled gp28 peptides in POPC/POPG liposomes. Spin-label (R1) is located at the indicated positions. All spectra were normalized to the highest spectral intensity.

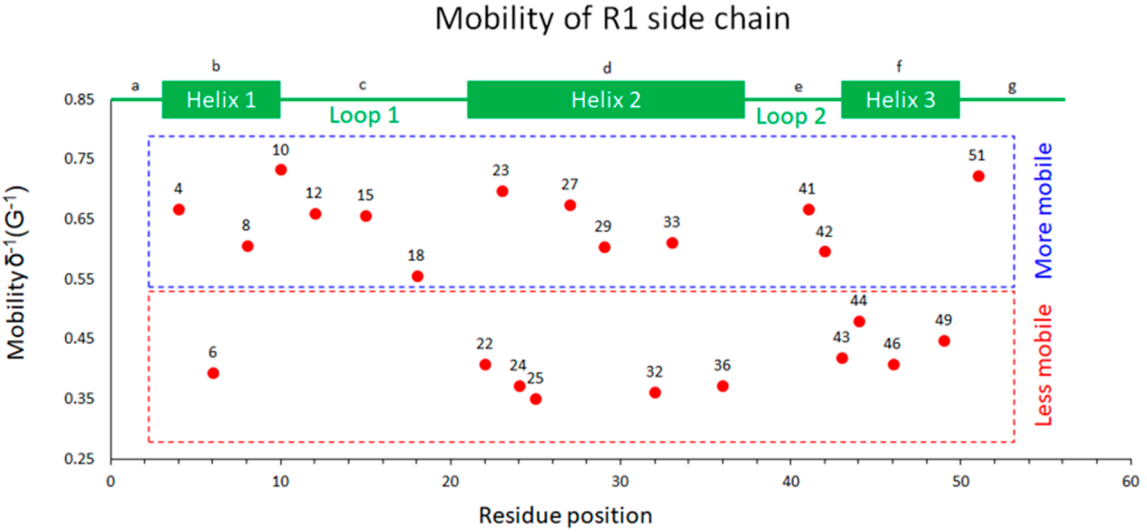

Figure 5. Relative mobility of R1 (δ^{-1}) as a function of residue positions in the primary sequence of gp28. A larger value of (δ^{-1}) indicates a higher mobility of the nitroxide spin-label at the corresponding position. Here, data points in the blue box represent more mobile residues while less mobile residues are in the red box. The different regions of the gp28 peptide are referred as (a) N-terminal side chain (1−2), (b) helix 1 (3−10), (c) loop 1 (11−20), (d) helix 2 (21−37), (e) loop 2 (38−42), (f) helix 3 (43−51), and (g) C-terminal side chain (52−56).

a significant effect on the global secondary structure of the gp28 constructs.

CW-EPR Spectral Line-Shape Analysis of gp28 in Proteoliposomes. Through CW-EPR spectral analysis of SL proteins, structural and dynamic properties can be probed at the residue-specific level with high spatial resolution.[37,53−56] A series of 23 CW-EPR spectra are presented in Figure 4 for spin-labeled gp28 constructs at different locations after incorporation into POPC/POPG proteoliposomes. Three ^{14}N hyperfine peaks of the R1 side chain attached to the peptide backbone were observed for all CW-EPR spectra. In the EPR spectrum of the unbound (low or no interaction with the membrane) points, the line width of the central peak is sharper than that of the bound ones, since a sharper peak indicates higher side chain (R1) mobility or less interaction with the membrane. In most EPR spectra, there is only one motional component, indicating monodispersity of conformational and motional properties. However, CW-EPR spectra of H18R1, G25R1, G36R1, and G32R1 exhibit a tinge of two spectral components (rigid and fast), which is indicative of heterogeneous components at these sites.[53] In addition to qualitative information, CW-EPR line-shape analysis can provide quantitative information about the dynamic behavior.[15,28,57,58] In Figure 5, the δ^{-1} of the central line width versus residue position shows the mobility of individual residues.

In Figure 5, except for K6R1, helix 1 (F4R1, L8R1, and A10R1) exhibits high mobility, like Loop1 (W12R1, T15R1, and H18R1) and Loop2 (Q41R1 and S42R1). For helix 2, L23R1, A27R1, R33R1, K34R1 showed higher mobility than I22R1, R24R1, G25R1, G32R1 and G36R1. For helix 3, A43R1, L46R1, and V49R1 showed lower mobility than

https://doi.org/10.1021/acs.jpcb.3c03679
J. Phys. Chem. B 2023, 127, 9236−9247

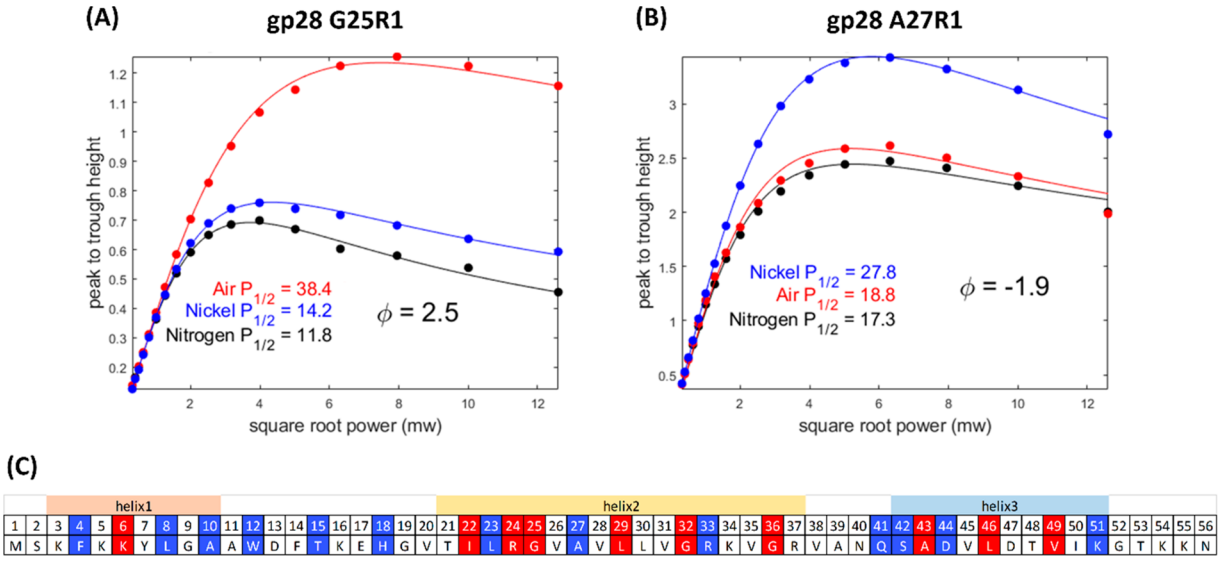

Figure 6. Representative CW-EPR power saturation curves of gp28 in POPC/POPG proteoliposomes. (A) Power saturation curves for gp28 G25R1 and (B) power saturation curves for gp28 A27R1. The blue circles represent NiEDDA, red circles represent oxygen, and black circles represent nitrogen spectra with their fitted lines from eq 3. The amplitudes of the first derivative $m_I = 0$ peak were plotted against the square root of the incident microwave (MW) power. (C) Color-coded primary sequence of gp28, where red represents residues buried in the lipid bilayer and blue represents solvent-exposed residues based on the CW-EPR power saturation data.

D44R1 and K51R1. A10R1 with an δ^{-1} of 0.73 G^{-1} was observed to have the highest mobility, while G25R1 in helix 2 had the lowest mobility of 0.35 G^{-1}. The δ^{-1} values for helix 1 range from 0.39 to 0.73 G^{-1}, for helix 2 range from 0.36 to 0.69 G^{-1}, and for helix 3 range from 0.40 to 0.72 G^{-1}. When compared with helix 1 and helix 3, the δ^{-1} values of helix 2 seem to change in a more periodic manner. The scaled mobility was shown (Figure S5) also resembles the pattern observed for the relative mobility (Figure 5).

Interaction of gp28 with the Lipid Bilayer from CW-EPR Power Saturation Experiments. CW-EPR power saturation is an effective and convenient biophysical technique for studying protein structure and topology with respect to lipid bilayer membranes.[23] CW-EPR power saturation experiments were conducted on 23 spin-labeled gp28 samples incorporated into the POPC/POPG proteoliposomes. A representative set of CW-EPR power saturation data is shown in Figure 6. In Figure 6A, according to the relative power saturation profile of the oxygen and NiEDDA spectra, A27R1 was more accessible to the polar relaxing reagent NiEDDA, whereas G25R1 was more accessible to the nonpolar oxygen. In view of this trend, it appears that residue A27R1 falls outside of the lipid bilayer, whereas residue G25R1 is located inside the lipid bilayer. Equation 4 was used to calculate the depth parameter (φ) for each residue in the membrane insertion quantitative analysis. The positive value of φ indicates that the side chain is buried inside the lipid bilayer, while the negative value indicates that the side chain is solvent-exposed.[7,23,59−61] According to the φ value measurements, residues buried in the lipid bilayer (Red residues) or exposed to the solvent (Blue residues) are shown in Figure 6C. (All power saturation data are presented in Supplementary Figure S3)

MD Simulation Data Analysis of gp28 in a Membrane. Building a topological model of a membrane associated protein by means of EPR spectroscopic data is quite challenging when no deposited structure is available. Previous characterization and secondary structural prediction indicated that it likely consisted of 3 amphipathic helices; however, there is no available information on tertiary structure or how stable these helices are, either in the membrane or in solution. As an amphipathic peptide, gp28 should exist in both a soluble and membrane-bound state.[12] For a more complete understanding of the peptide, we wanted to model it in both states as well as the transition between them as adsorption occurs. Because gp28 does not have a published structure, we needed to develop a structural model. gp28 has previously been predicted to have a secondary structure consisting of 3 helices, and our CD data indicate that gp28 mostly is helical and may have some random coils.[12] As such, we modeled the peptide as containing a short N-terminal helix, a longer middle helix and a 1.5 turn C-terminal helix connected by random coil and followed by a disordered C-terminal tail, at appropriately the boundaries of the previously published predicted secondary structural elements.[12] The model built in this way, however, is simply an educated guess, but with the large portion of random coil in the model, it is unlikely to have a single well-defined fold. To sample a wide range of conformational states that could be adopted and build a robust model, we generated 10 different starting structures by randomizing the backbone angles of the residues built as loops. Each of these was subjected to their own minimization, equilibration, and production MD in an explicitly solvated water box and allowed to run for 100 ns to observe the stability of helices and how they moved relative to one another.[62,63] In solution, helix 1 was fairly unstructured and frequently unraveled, unless stabilized by maintaining contact with the two other helices. To minimize its radius of gyration, extended starting poses collapsed inward as helix 1 and helix 3 associated with helix 2. Extended conformations tended to fold inward to maximize contact of helix 1 and helix 3 with helix 2. The orientations of these contacts were observed to be fairly fluid, and helices 1 and 3 reoriented themselves multiple times within the production run when they were not adsorbed. In 5 of the runs it was observed that helices 1 or 3 could initiate contact with the membrane and anchor the peptide by lying

https://doi.org/10.1021/acs.jpcb.3c03679
J. Phys. Chem. B 2023, 127, 9236−9247

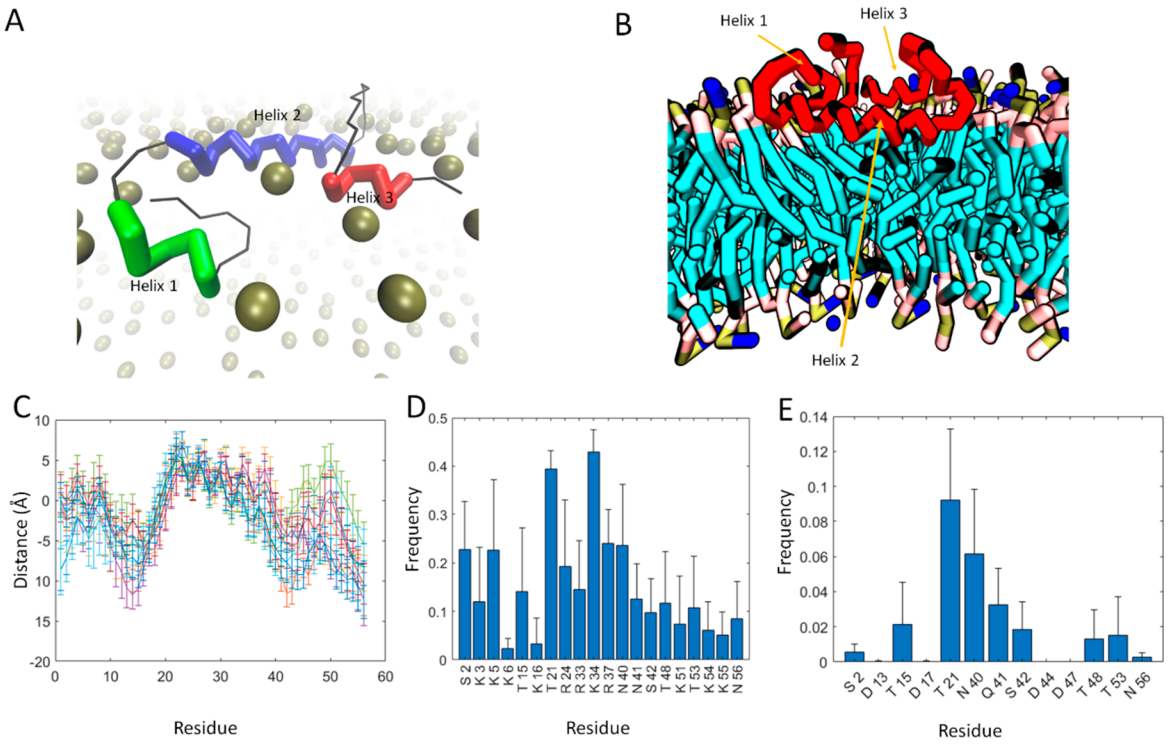

Figure 7. Representative structure of gp28 from molecular dynamic simulations. (A) The top-down view of gp28: gold spheres represent the phospholipid headgroup, green helix represents helix 1, blue helix represents helix 2, red helix represents helix 3, loops and unstructured regions are presented in black. (B) The side view of gp28 while incorporated into lipid bilayer: gp28 is presented in red, cyan structure represents lipid chains, blue, pink, and olive-green structures represent the phospholipid head groups. Side chains are not shown for gp28. (C) Mean depth of the α carbon of each residue beneath the surrounding phosphates, with replicate trajectories overlaid. Bars indicate standard deviation. (D) Time averaged frequency for which positive and partially positive side chain beads were in contact with PO_4 beads. (E) Time averaged frequency for which negative and partially negative side chain beads were in contact with choline beads.

perpendicular to the membrane normal; however, these states were transient, and stable adsorption was characterized by the incorporation of helix 2 lying mostly perpendicular to the membrane normal, which occurred in 8 of the 10 runs. All runs in which stable adsorption occurred showed residue 22 or 23 as the most deeply buried beneath the phosphate head groups, with helix 2 rising at a low angle such that in 4 of the runs the mean depth of the C-terminal end of helix 2 rose above the plane of the phosphate groups (Figure 7C–E). Helices 1 and 3 showed more variability in their depth but generally positioned themselves several Å above the phosphates lying mostly flat against the membrane surface. The loop region between helices 1 and 2 and the loosely structured C-terminus were the most lipophobic, extending well into the aqueous region. The relative orientation of helices when adsorbed varied considerably between runs.[64,65] (Supplementary Video V1)

Unsurprisingly for a peptide with a +7 charge at neutral pH, Arg and Lys side chains formed significant electrostatic interactions with the negatively charged phosphates of the lipids, as did polar residues. K34 had the most stable interaction with the phosphates, being within a 4 Å radius of a phosphate in 42% of frames after stable adsorption had occurred. Electrostatic interactions were more stable over helix 2 than for helices one or three, which likely explains the greater variance in C-alpha depths seen for these helices. In *E. coli* most lipids have a net neutral charge, with the negative charge from the phosphate balanced by the positive charge from the ethanolamine of POPE.[65] In our simulations, however, negatively charged and polar side chains showed only transient interaction with the positive choline headgroups of POPC (Figure 7A,B). This is in part due to their lower abundance than phosphates as half of the lipid composition was POPG in the simulations. Even so, it is likely the case that the phosphate interactions are a stronger driving factor in adsorption since the average charge over the membrane surface is negative. One notable finding is the stability of T21 hydroxyl electrostatic interactions. The partial positive charge on the side chain had the second highest residence within the 4 Å phosphate probe radius and surprisingly was more stably in contact with phosphate than any basic residue with a formal positive charge except K34, and notably the partial negative end of this dipole also showed the most contact with choline. Given its position close to the deepest point within the membrane on the first turn of helix 2, this suggests that it may be functionally important.

DISCUSSION

This is the first biophysical study of gp28 that uses EPR spectroscopic techniques coupled to MD simulation to illustrate the relative differences in the dynamics of different segments and residues. Using the quantitative and qualitative data presented in this study, we will be able to gain a deeper understanding of the side-chain dynamics and structural topology of gp28 in proteoliposomes. The library of CW-EPR spectra shows that most of the gp28 constructs show single mobility components, while some show multiple lineshape components in their CW-EPR spectra (Figure 4). The presence of two motional components in the CW-EPR spectra for H18R1, G25R1, and G32R1 can be attributed to their

https://doi.org/10.1021/acs.jpcb.3c03679
J. Phys. Chem. B 2023, 127, 9236−9247

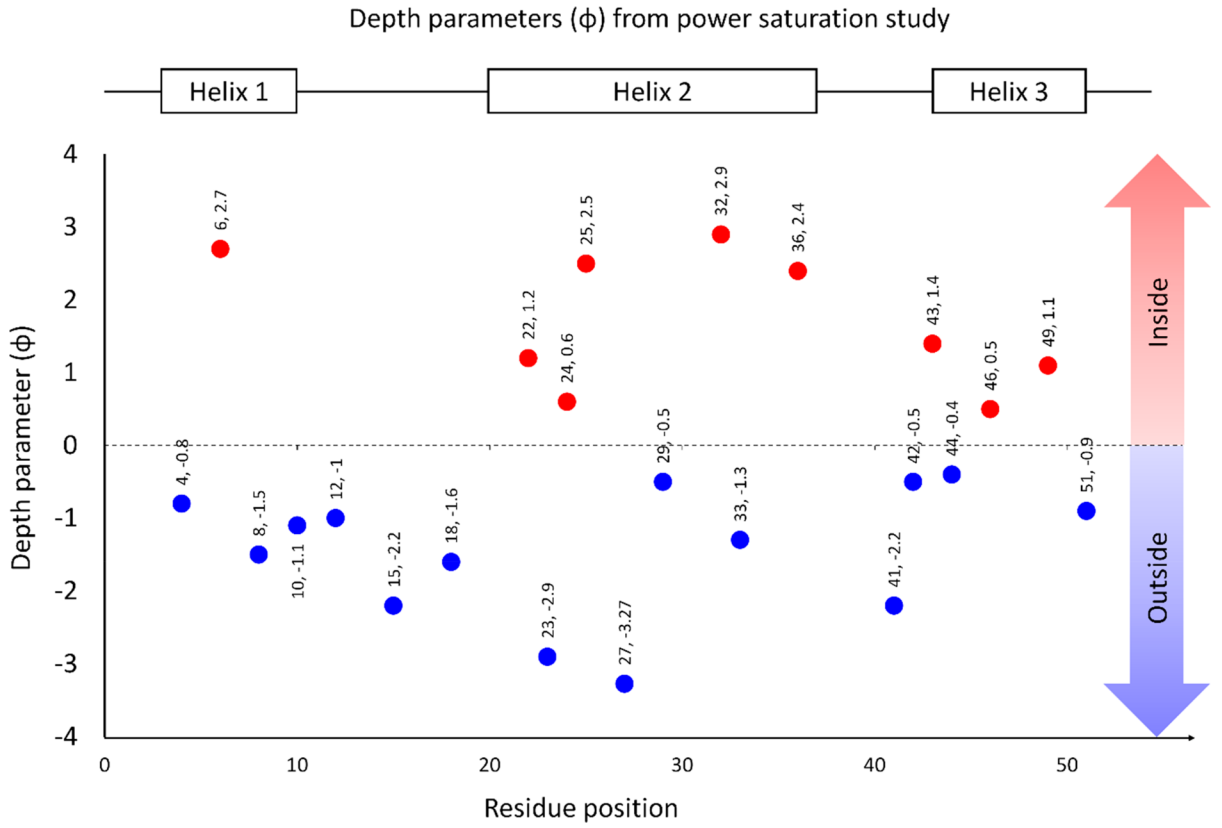

Figure 8. Calculated depth parameter (φ) for different positions of gp28 as a function of residue positions in the POPC/POPG proteoliposomes. Positive (φ) values (red) indicate that the R1 side chains are embedded inside the lipid bilayer and negative (φ) values (blue) indicate that the R1 side chains are solvent-exposed.

positions and side chains on the same side of the helix.[28,57] As a result of a heterogeneous interaction with the local environment, the R1 side chain shows different spectral components.[57] Two components of G25R1 and G32R1 may also be explained by bulky side chains on the same side of the helix (3 or 4 residues away from R1) that give characteristic anisotropic motion of the spin-label. For H18R1, the two components may rise from the bulky side chain of histidine or other bulky side chains nearby.[7,28,57] From the distribution of mobility (Figure 5), we can categorize the gp28 constructs into two categories: (a) more mobile and (b) less mobile. A possible explanation for the points showing higher mobility is that they remain outside the membrane and exposed to the solvent. Thus, the spin-labels attached to these points move more freely compared to the membrane embedded points of gp28 peptide.[8] Among the three helices, helix 1 (average mobility for helix 1, $\overline{\delta}_{\text{helix 1}} = 0.60$) showed higher average mobility when compared to helix 2 ($\overline{\delta}_{\text{helix 2}} = 0.50$) and helix 3 ($\overline{\delta}_{\text{helix 3}} = 0.51$). This indicates that the interaction of helix 1 with the proteoliposomes is less prominent than other helices. Also, the loop regions ($\overline{\delta}_{\text{loop}} = 0.63$) showed higher mobility compared to the helices ($\overline{\delta}_{\text{helices}} = 0.54$).

In addition to analyzing the mobility in the CW-EPR spectra, the depth parameter values (φ) obtained from power saturation experiments provide important insights into the peptide's topology with respect to the membrane. Figure 8 displays the depth parameter values for various residue positions of the gp28 peptide, which were obtained from the CW-EPR power saturation experiments. Most of the residues in helix 1 have negative φ values ($\varphi_{\text{F4C}} = -0.8$, $\varphi_{\text{L8C}} = -1.5$, and $\varphi_{\text{A10C}} = -1.1$), except for one residue ($\varphi_{\text{K6C}} = 2.7$), which suggests that most points on the helix 1 are exposed to the solvent.[7] On the other hand, in helix 2, the residues with positive φ values ($\varphi_{\text{I22C}} = 1.2$, $\varphi_{\text{R24C}} = 0.6$, $\varphi_{\text{G25C}} = 2.5$, $\varphi_{\text{G32C}} = 2.9$, and $\varphi_{\text{G36C}} = 2.4$) and those with negative φ values ($\varphi_{\text{L23C}} = -2.9$, $\varphi_{\text{A27C}} = -3.3$, $\varphi_{\text{L29C}} = -0.5$, and $\varphi_{\text{R33C}} = -1.3$) are evenly distributed in terms of their numbers. Helix 3 also demonstrates a balanced distribution between the quantities of residues that exhibit positive φ values ($\varphi_{\text{A43C}} = 1.4$, $\varphi_{\text{L46C}} = 0.5$, and $\varphi_{\text{V49C}} = 1.1$) and those that exhibit negative φ values ($\varphi_{\text{S42C}} = -0.5$, $\varphi_{\text{D44C}} = -0.4$, and $\varphi_{\text{K51C}} = -0.9$). Regarding the residues studied in the loop regions, it is mostly observed that they exhibit negative φ values located outside the membrane. The depth parameter values obtained from power saturation experiments are consistent with the mobility parameters derived from the CW-EPR line shape analysis. The power saturation data confirmed the membrane interaction of helices 2 and 3 while the helix 1, and loop regions failed to confirm any clear interaction.

Based on the depth parameter values (φ), the relative orientation of each residue and their interaction with respect to the lipid bilayer are determined. For helix 2 and helix 3, the even distribution of residues with positive φ values and those with negative φ values suggests that some of the residues are located inside the membrane, while others are solvent-exposed.[8,43] The R1 side chains are embedded inside the lipid bilayer when the φ values are positive, while the R1 side chains are exposed to solvent when the φ values are negative.[7,37,59] Based on the depth parameters, it is evident that the accessibility data exhibit periodic oscillations for

https://doi.org/10.1021/acs.jpcb.3c03679
J. Phys. Chem. B 2023, 127, 9236−9247

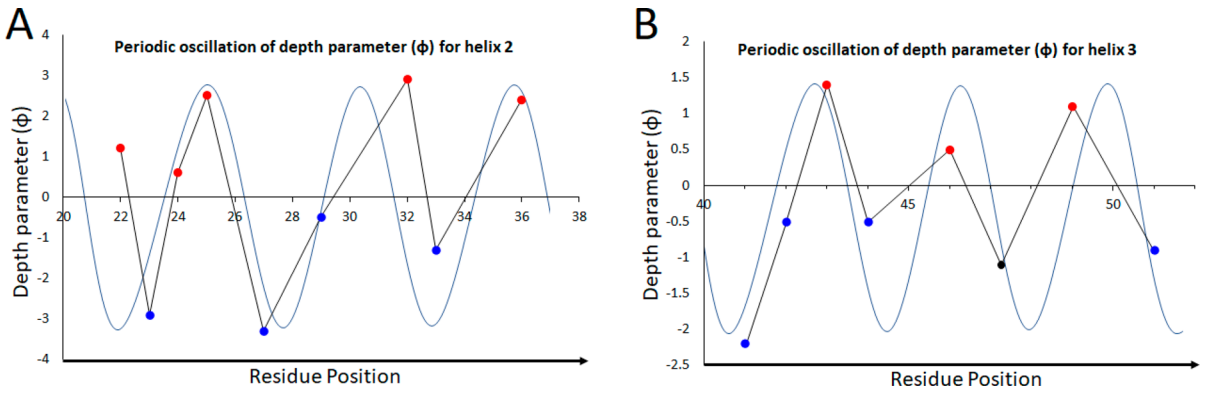

Figure 9. (A) Periodic oscillation of depth parameters along labeling position, representing helix 2, depicted by a sinusoidal line (for residues 22−36). (B) The periodic oscillation of depth parameters (for residues 41−51) corresponding to the helix 3 as a function of labeling position as illustrated with the sinusoidal line.[59] The sinusoidal lines have a periodicity consistent with the helical register of an α helix lying parallel with the membrane surface.[43,59] Values of φ that are positive (shown in red) indicate that the R1 side chains are located within the lipid bilayer, while values that are negative (shown in blue) indicate that the R1 side chains are exposed to the solvent.

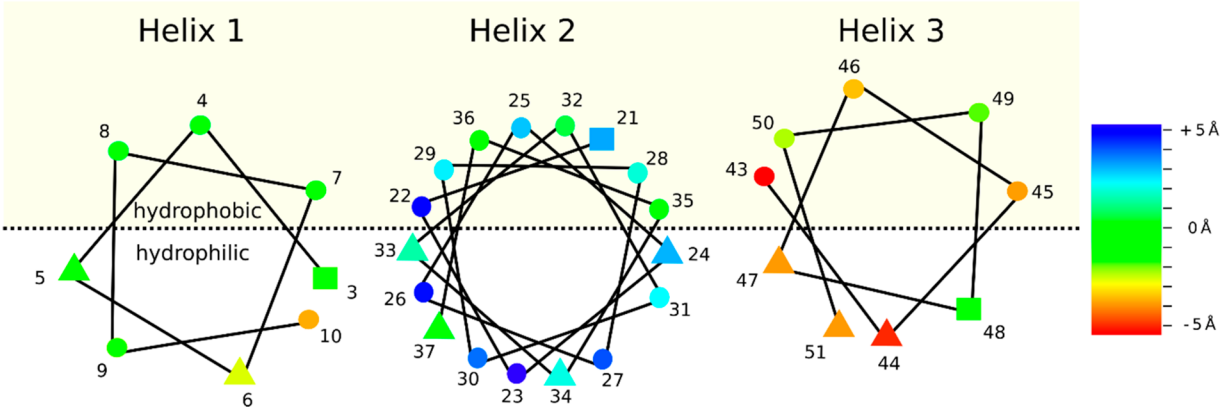

Figure 10. Helical wheel plot based on the power saturation data, wheel prediction software and previous publication.[12,67] Polar residues are represented as squares, charged residues as triangles, and nonpolar residues as circles. Residues are color coded according to the mean depth of the backbone beneath the surrounding lipid phosphates across MD trajectories, as shown in Figure 7C. The dashed line separates predicted hydrophobic and hydrophilic faces of each helix.

helices 2 and 3 (Figure 9A,B). These periodic oscillations are similar to the periodicity observed in the sinusoidal lines, which correspond to the pattern of an α helix lying on the membrane surface indicating the presence of an amphipathic-helical structure.[59] Moreover, the comparison of the depth parameter pattern with the sinusoidal curve (Figure 9B) indicates that helix 3 may start from the 41st position instead of the 43rd position predicted by the Ry young group.[12,59]

CW-EPR Power saturation data when combined with the helical wheel plot of an α helix can provide important insight about how the helices are incorporated within the membrane. Figure 10 represents the helical wheel plots for all three helices, demonstrating the hydrophilic and hydrophobic sides of the helices. For helix 2, the local maxima (residues 25, 32, and 36; red circles) observed in Figure 9A correspond to the lipid-exposed residues are also observed to cluster together on the hydrophobic side of the helical wheel in Figure 10B. Conversely, the local minima (23, 27, and 33; blue circles; Figure 9A) of helix 2 correspond to the solvent-exposed residues that appear toward the hydrophilic face of the helical wheel (Figure 10B). For helix 3, the local maxima (residues 43, 46, and 49; red circles; Figure 9B) represent the lipid-exposed residues facing the hydrophobic side of a helical wheel, and local minima (41, 44, and 51; blue circles; Figure 9B) correspond to the solvent-exposed residues facing the opposite side of the helical wheel (Figure 10C). These findings provide additional evidence for the existence of amphipathic-helical structures in the peptide.[59] However, the hydrophobic residues represented in the helical wheel plot for helix 1 did not show any interaction with the membrane (Figures 8 and 10A). This indicates that helix 1 may remain fully exposed to the solvent or may have some electrostatic interaction with the phosphate head groups in the hydrophilic region. The only positive φ value observed in the power saturation experiment for K6C in helix 1 can be attributed to the mutational effect.[5,9] Replacing lysine (a polar, positively charged amino acid at pH 7) with cysteine (a polar, uncharged amino acid at pH 7) can lead to changes in the hydrophobicity of a peptide. Therefore, when a lysine residue is replaced by cysteine, it can potentially increase the hydrophobicity of the peptide that may influence the depth parameter of the residue position.[5,9,66]

A point of contrast exists between the measured depth parameter and the mean depth of the peptide backbone at that position, as seen in the MD trajectories. In MD trajectories, backbone positions for helix 2 along both faces are submerged beneath the phosphate of the lipids and emerge above the phosphates in the last turn of the helix. Backbone positions in helix 3 remain above the phosphates. The power saturation for

https://doi.org/10.1021/acs.jpcb.3c03679
J. Phys. Chem. B 2023, 127, 9236−9247

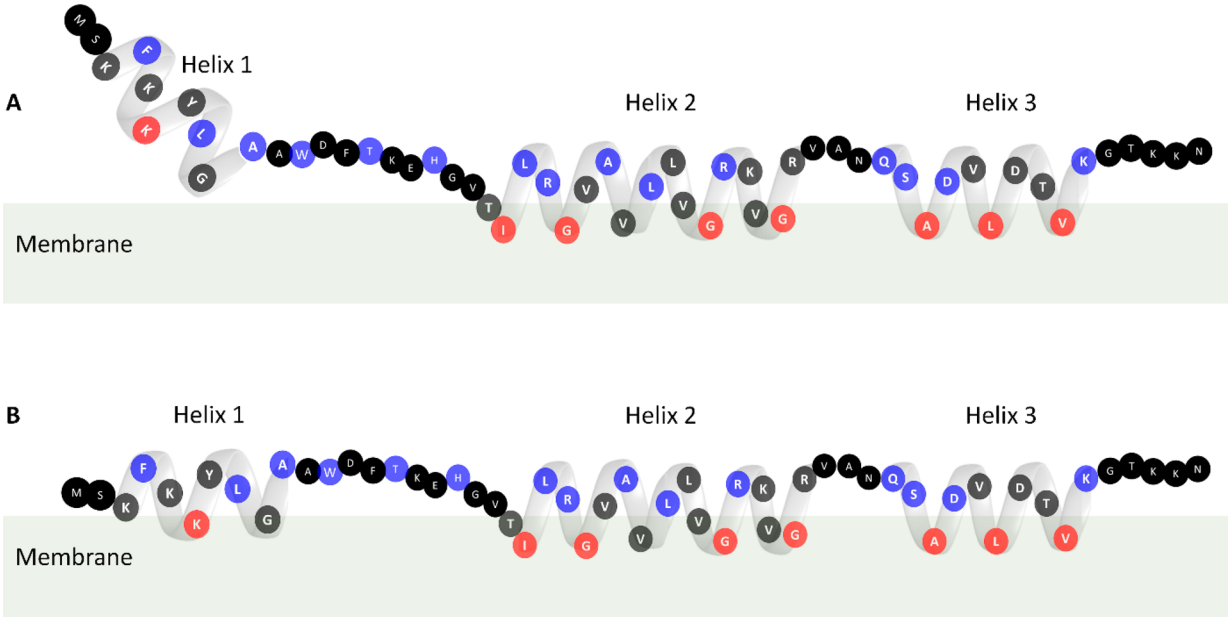

Figure 11. Structural topology model of gp28 based on the CW-EPR line shape analysis and power saturation data. (A) This model represents that helix 1 is fully exposed to the solvent, while helix 2 and helix 3 interact with the membrane. (B) gp28 model represents all three helices interacting with the membrane. The residues are color-coded based on power saturation data. Blue represents solvent-exposed residues, red represents residues interacting with lipid bilayers, and black represents residues not studied by power saturation. Olive-green represents the phospholipid bilayer.

helices 2 and 3 alternates between positive and negative depth parameters and does not capture the rising tilt of helix 2 or the difference in the average depth of helix 2 compared to that of helix 3. What is important to note is that MTSL linked by disulfide to a cysteine creates a highly flexible linker between the nitroxide radical producing the EPR signal and the backbone, leading to a significant distance between the two and considerable uncertainty in their relative positions. This makes it difficult to utilize the depth parameters from EPR as quantitative restraints on the depth of the backbone at a given site in MD simulations. While the EPR data do not reproduce these trends seen in MD, the inherent uncertainty in label positions also means that the two are still compatible with each other. The most important aspect in which they corroborate each other is that the helices are amphipathic and lie close to 90° relative to the membrane normal in generally close proximity to the phosphate headgroups.

Based on the dynamic information and accessibility data reported in this study, two structural topology models of gp28 are proposed (Figure 11). The residues in Figure 11 are color-coded based on CW-EPR power saturation data, with blue representing solvent-exposed residues, red representing residues interacting with the lipid bilayer, and black representing residues that have not been studied by CW-EPR power saturation. Several residues are labeled with residue positions as a visualization guide. The helical tilt of helix 2 and helix 3 is proposed based on the possible positive hydrophobic mismatch. To confirm the proposed topology of gp28 and the relative orientation of the helices in the presence of a lipid bilayer, further structural studies are needed.[68]

The simulation data also suggest that helix 2 interacts stably with the phospholipid membrane bilayer. However, helix 1 was fairly unstructured and frequently unraveled, unless stabilized by maintaining contact with the other two helices. Helix 2 was observed to be almost perpendicular to the membrane normal, and stable adsorption occurred when it is incorporated into the membrane. Significant electrostatic interactions were observed between positively charged residues and negatively charged phosphates in the membrane. The hydroxyl group of T21 was found to be stably in contact with the phosphate, suggesting that this position may be functionally important.

CONCLUSION

This study reported the structural dynamics and topology of the gp28 incorporated into a POPC/POPG lipid bilayer using EPR spectroscopic techniques. Spin-label positions were selected judiciously to minimize structural perturbation, while gaining maximum information on structural dynamics and topology of gp28. The CD data confirmed that gp28 maintains a predicted native α-helical secondary structure. In this study, we found that helix 1 may remain fully exposed to the solvent or may have some electrostatic interaction with lipid head groups, while the interaction of helix 2 and helix 3 with the lipid bilayer is evident. The proposed structural topology model of gp28 may help in future studies of gp28 and other amphipathic surface-bound proteins. Further structural studies are needed to confirm the proposed topology and relative orientation of the helices in the presence of a lipid bilayer.

ASSOCIATED CONTENT

Supporting Information

The Supporting Information is available free of charge at https://pubs.acs.org/doi/10.1021/acs.jpcb.3c03679.

Mass spectrum, MIC test, CW-EPR power saturation, DLS, relative mobility, depth parameters (PDF)
Molecular dynamic simulation (MPG)

AUTHOR INFORMATION

Corresponding Author

Gary A. Lorigan − *Department of Chemistry and Biochemistry, Miami University, Oxford, Ohio 45056, United*

https://doi.org/10.1021/acs.jpcb.3c03679
J. Phys. Chem. B 2023, 127, 9236−9247

States; orcid.org/0000-0002-2395-3459; Phone: (513) 529-2813; Email: gary.lorigan@miamioh.edu; Fax: (513) 529-5715

Authors

Rasal H. Khan − *Department of Chemistry and Biochemistry, Miami University, Oxford, Ohio 45056, United States*

Nancy C. Rotich − *Department of Chemistry and Biochemistry, Miami University, Oxford, Ohio 45056, United States*

Andrew Morris − *Department of Chemistry and Biochemistry, Miami University, Oxford, Ohio 45056, United States*

Tanbir Ahammad − *Department of Chemistry and Biochemistry, Miami University, Oxford, Ohio 45056, United States*

Binaya Baral − *Department of Chemistry and Biochemistry, Miami University, Oxford, Ohio 45056, United States*

Indra D. Sahu − *Natural Science Division, Campbellsville University, Campbellsville, Kentucky 42718, United States;* orcid.org/0000-0002-7333-0356

Complete contact information is available at: https://pubs.acs.org/10.1021/acs.jpcb.3c03679

Notes

The authors declare no competing financial interest.

■ ACKNOWLEDGMENTS

This work was generously supported by the NSF CHE-2305834 grant and Miami University.

■ REFERENCES

(1) Suttle, C. A. Viruses in the Sea. *Nature* **2005**, *437*, 356.

(2) Cahill, J.; Young, R. Phage Lysis: Multiple Genes for Multiple Barriers. *Adv. Virus Res.* **2019**, *103*, 33−70.

(3) Young, R. *Phage Lysis: Three Steps, Three Choices, One Outcome* **2014**, *52* (3), 243−258.

(4) Pang, T.; Savva, C. G.; Fleming, K. G.; Struck, D. K.; Young, R. *Structure of the Lethal Phage Pinhole.* **2009**, *106*, 18966.

(5) Pang, T.; Park, T.; Young, R. *Mutational Analysis of the S 21 Pinholin.* **2010**, *76* (February), 68−77.

(6) Savva, C. G.; Dewey, J. S.; Moussa, S. H.; To, K. H.; Holzenburg, A.; Young, R. Stable Micron-Scale Holes Are a General Feature of Canonical Holins. *Mol. Microbiol.* **2014**, *91* (1), 57−65.

(7) Ahammad, T.; Drew, D. L.; Sahu, I. D.; Serafin, R. A.; Clowes, K. R.; Lorigan, G. A. Continuous Wave Electron Paramagnetic Resonance Spectroscopy Reveals the Structural Topology and Dynamic Properties of Active Pinholin S2168 in a Lipid Bilayer. *J. Phys. Chem. B* **2019**, *123* (38), 8048−8056.

(8) Ahammad, T.; Drew, D. L.; Khan, R. H.; Sahu, I. D.; Faul, E.; Li, T.; Lorigan, G. A. Structural Dynamics and Topology of the Inactive Form of S21Holin in a Lipid Bilayer Using Continuous-Wave Electron Paramagnetic Resonance Spectroscopy. *J. Phys. Chem. B* **2020**, *124* (26), 5370−5379.

(9) Ahammad, T.; Khan, R. H.; Sahu, I. D.; Drew, D. L.; Faul, E.; Li, T.; McCarrick, R. M.; Lorigan, G. A. Pinholin S21 Mutations Induce Structural Topology and Conformational Changes. *Biochim. Biophys. Acta - Biomembr.* **2021**, *1863* (12), No. 183771.

(10) Young, R. Phage Lysis: Do We Have the Hole Story Yet? *Curr. Opin. Microbiol.* **2013**, *16* (6), 790−797.

(11) Berry, J.; Rajaure, M.; Pang, T.; Young, R. The Spanin Complex Is Essential for Lambda Lysis. *J. Bacteriol.* **2012**, *194* (20), 5667−5674.

(12) Holt, A.; Cahill, J.; Ramsey, J.; Martin, C.; O'Leary, C.; Moreland, R.; Maddox, L. T.; Galbadage, T.; Sharan, R.; Sule, P.; Cirillo, J. D.; Young, R. Phage-Encoded Cationic Antimicrobial Peptide Required for Lysis. *J. Bacteriol.* **2021**, *204* (1), JB0021421.

(13) Knirel, Y. A.; Prokhorov, N. S.; Shashkov, A. S.; Ovchinnikova, O. G.; Zdorovenko, E. L.; Liu, B.; Kostryukova, E. S.; Larin, A. K.; Golomidova, A. K.; Letarov, A. V. Variations in O-Antigen Biosynthesis and O-Acetylation Associated with Altered Phage Sensitivity in Escherichia Coli 4s. *J. Bacteriol.* **2015**, *197* (5), 905−912.

(14) Zhang, L.; Rozek, A.; Hancock, R. E. W. Interaction of Cationic Antimicrobial Peptides with Model Membranes. *J. Biol. Chem.* **2001**, *276* (38), 35714−35722.

(15) Columbus, L.; Hubbell, W. L. A New Spin on Protein Dynamics. *Trends Biochem. Sci.* **2002**, *27* (6), 288−295.

(16) Ishima, R.; Freedberg, D. I.; Wang, Y. X.; Louis, J. M.; Torchia, D. A. Flap Opening and Dimer-Interface Flexibility in the Free and Inhibitor- Bound HIV Protease, and Their Implications for Function. *Structure* **1999**, *7* (9), 1047−1055.

(17) Volkman, B. F.; Lipson, D.; Wemmer, D. E.; Kern, D. Two-State Allosteric Behavior in a Single-Domain Signaling Protein. *Science (80-.)* **2001**, *291* (5512), 2429−2433.

(18) Mulder, F. A. A.; Mittermaier, A.; Hon, B.; Dahlquist, F. W.; Kay, L. E. Studying excited states of proteins by NMR spectroscopy. *Nat. Struct Biol.* **2001**, *8*, 932−935.

(19) Rozovsky, S.; Jogl, G.; Tong, L.; McDermott, A. E. Solution-State NMR Investigations of Triosephosphate Isomerase Active Site Loop Motion: Ligand Release in Relation to Active Site Loop Dynamics. *J. Mol. Biol.* **2001**, *310* (1), 271−280.

(20) Bates, I. R.; Boggs, J. M.; Feix, J. B.; Harauz, G. Membrane-Anchoring and Charge Effects in the Interaction of Myelin Basic Protein with Lipid Bilayers Studied by Site-Directed Spin Labeling. *J. Biol. Chem.* **2003**, *278* (31), 29041−29047.

(21) Klug, C. S.; Feix, J. B. Methods and Applications of Site-Directed Spin Labeling EPR Spectroscopy. *Methods Cell Biol.* **2008**, *84* (07), 617−658.

(22) Altenbach, C.; Marti, T.; Khorana, H. G.; Hubbell, W. L. Transmembrane Protein Structure: Spin Labeling of Bacteriorhodopsin Mutants. *Science (80-.)* **1990**, *248* (4959), 1088−1092.

(23) Altenbach, C.; Greenhalgh, D. A.; Khorana, H. G.; Hubbell, W. L. A Collision Gradient Method to Determine the Immersion Depth of Nitroxides in Lipid Bilayers: Application to Spin-Labeled Mutants of Bacteriorhodopsin. *Proc. Natl. Acad. Sci. U. S. A.* **1994**, *91* (5), 1667−1671.

(24) Sahu, I. D.; McCarrick, R. M.; Lorigan, G. A. Use of Electron Paramagnetic Resonance to Solve Biochemical Problems. *Biochemistry* **2013**, *52* (35), 5967−5984.

(25) Altenbach, C.; Froncisz, W.; Hemker, R.; Mchaourab, H.; Hubbell, W. L. Accessibility of Nitroxide Side Chains: Absolute Heisenberg Exchange Rates from Power Saturation EPR. *Biophys. J.* **2005**, *89* (3), 2103−2112.

(26) Pyka, J.; Ilnicki, J.; Altenbach, C.; Hubbell, W. L.; Froncisz, W. Accessibility and Dynamics of Nitroxide Side Chains in T4 Lysozyme Measured by Saturation Recovery EPR. *Biophys. J.* **2005**, *89* (3), 2059−2068.

(27) Hubbell, W. L.; Altenbach, C. Investigation of Structure and Dynamics in Membrane Proteins Using Site-Directed Spin Labeling. *Curr. Opin. Struct. Biol.* **1994**, *4* (4), 566−573.

(28) Hubbell, W. L.; Mchaourab, H. S.; Altenbach, C.; Lietzow, M. A. Watching Proteins Move Using Site-Directed Spin Labeling. *Structure* **1996**, *4* (7), 779−783.

(29) Hubbell, W. L.; Gross, A.; Langen, R.; Lietzow, M. A. Recent Advances in Site-Directed Spin Labeling of Proteins. *Curr. Opin. Struct. Biol.* **1998**, *8*, 649−656.

(30) Hubbell, W. L.; Cafiso, D. S.; Altenbach, C. Identifying Conformational Changes with Site-Directed Spin Labeling. *Nat. Struct. Biol.* **2000**, *7* (9), 735−739.

(31) Chandrudu, S.; Simerska, P.; Toth, I. Chemical Methods for Peptide and Protein Production. *Molecules* **2013**, *18* (4), 4373−4388.

(32) Sahu, I. D.; Lorigan, G. A. Site-Directed Spin Labeling EPR for Studying Membrane Proteins. *Biomed Res. Int.* **2018**, *2018* (1), 1.

(33) Drew, D. L.; Ahammad, T.; Serafin, R. A.; Butcher, B. J.; Clowes, K. R.; Drake, Z.; Sahu, I. D.; McCarrick, R. M.; Lorigan, G. A.

Solid Phase Synthesis and Spectroscopic Characterization of the Active and Inactive Forms of Bacteriophage S21 Pinholin Protein. *Anal. Biochem.* **2019**, *567* (December 2018), 14−20.
(34) Bottorf, L.; Sahu, I. D.; McCarrick, R. M.; Lorigan, G. A. Utilization of 13C-Labeled Amino Acids to Probe the α-Helical Local Secondary Structure of a Membrane Peptide Using Electron Spin Echo Envelope Modulation (ESEEM) Spectroscopy. *Biochim. Biophys. Acta - Biomembr.* **2018**, *1860* (7), 1447−1451.
(35) Mayo, D. J.; Sahu, I. D.; Lorigan, G. A. Assessing Topology and Surface Orientation of an Antimicrobial Peptide Magainin 2 Using Mechanically Aligned Bilayers and Electron Paramagnetic Resonance Spectroscopy. *Chem. Phys. Lipids* **2018**, *213* (April), 124−130.
(36) White, G. F.; Schermann, S. M.; Bradley, J.; Roberts, A.; Greene, N. P.; Berks, B. C.; Thomson, A. J. Subunit Organization in the TatA Complex of the Twin Arginine Protein Translocase: A Site-Directed EPR Spin Labeling Study. *J. Biol. Chem.* **2010**, *285* (4), 2294−2301.
(37) Sahu, I. D.; Craig, A. F.; Dunagan, M. M.; Troxel, K. R.; Zhang, R.; Meiberg, A. G.; Harmon, C. N.; McCarrick, R. M.; Kroncke, B. M.; Sanders, C. R.; et al. Probing Structural Dynamics and Topology of the KCNE1Membrane Protein in Lipid Bilayers via Site-Directed Spin Labeling and Electron Paramagnetic Resonance Spectroscopy. *Biochemistry* **2015**, *54* (41), 6402−6412.
(38) Boggs, J. M.; Moscarello, M. A. Effect of Basic Protein from Human Central Nervous System Myelin on Lipid Bilayer Structure. *J. Membr. Biol.* **1978**, *39* (1), 75−96.
(39) Eletr, S.; Keith, A. D. Spin-Label Studies of Dynamics of Lipid Alkyl Chains in Biological Membranes: Role of Unsaturated Sites. *Proc. Natl. Acad. Sci. U. S. A.* **1972**, *69* (6), 1353−1357.
(40) Yu, L.; Wang, W.; Ling, S.; Liu, S.; Xiao, L.; Xin, Y.; Lai, C.; Xiong, Y.; Zhang, L.; Tian, C. CW-EPR Studies Revealed Different Motional Properties and Oligomeric States of the Integrin B1a Transmembrane Domain in Detergent Micelles or Liposomes. *Sci. Rep.* **2015**, *5*, 1−11.
(41) Popp, C. A.; Hyde, J. S. Effects of Oxygen on EPR Spectra of Nitroxide Spin-Label Probes of Model Membranes. *J. Magn. Reson.* **1981**, *43* (2), 249−258.
(42) Klug, C. S.; Su, W.; Feix, J. B. Mapping of the Residues Involved in a Proposed β-Strand Located in the Ferric Enterobactin Receptor FepA Using Site-Directed Spin-Labeling. *Biochemistry* **1997**, *36* (42), 13027−13033.
(43) Pitt, T. *Methods in Molecular Biology. Volume 145. Bacterial Toxins. Methods and Protocols* **2001**, *47*, 503.
(44) Marrink, S. J.; Risselada, H. J.; Yefimov, S.; Tieleman, D. P.; De Vries, A. H. The MARTINI Force Field: Coarse Grained Model for Biomolecular Simulations. *J. Phys. Chem. B* **2007**, *111* (27), 7812−7824.
(45) Lee, J.; Cheng, X.; Swails, J. M.; Yeom, M. S.; Eastman, P. K.; Lemkul, J. A.; Wei, S.; Buckner, J.; Jeong, J. C.; Qi, Y.; et al. CHARMM-GUI Input Generator for NAMD, GROMACS, AMBER, OpenMM, and CHARMM/OpenMM Simulations Using the CHARMM36 Additive Force Field. *J. Chem. Theory Comput.* **2016**, *12* (1), 405−413.
(46) Hsu, P.-C.; Bruininks, B. M. H.; Jefferies, D.; Cesar Telles de Souza, P.; Lee, J.; Patel, D. S.; Marrink, S. J.; Qi, Y.; Khalid, S.; Im, W. Charmm-Gui Martini Maker for Modeling and Simulation of Complex Bacterial Membranes with Lipopolysaccharides. *J. Comput. Chem.* **2017**, *38* (27), 2354−2363.
(47) Qi, Y.; Ingólfsson, H. I.; Cheng, X.; Lee, J.; Marrink, S. J.; Im, W. CHARMM-GUI Martini Maker for Coarse-Grained Simulations with the Martini Force Field. *J. Chem. Theory Comput.* **2015**, *11* (9), 4486−4494.
(48) Pettersen, E. F.; Goddard, T. D.; Huang, C. C.; Couch, G. S.; Greenblatt, D. M.; Meng, E. C.; Ferrin, T. E. UCSF Chimera - A Visualization System for Exploratory Research and Analysis. *J. Comput. Chem.* **2004**, *25* (13), 1605−1612.
(49) Ting, D.; Wang, G.; Shapovalov, M.; Mitra, R.; Jordan, M. I.; Dunbrack, R. L. Neighbor-Dependent Ramachandran Probability Distributions of Amino Acids Developed from a Hierarchical Dirichlet Process Model. *PLoS Comput. Biol.* **2010**, *6* (4), e1000763.
(50) Pronk, S.; Páll, S.; Schulz, R.; Larsson, P.; Bjelkmar, P.; Apostolov, R.; Shirts, M. R.; Smith, J. C.; Kasson, P. M.; Van Der Spoel, D.; et al. GROMACS 4.5: A High-Throughput and Highly Parallel Open Source Molecular Simulation Toolkit. *Bioinformatics* **2013**, *29* (7), 845−854.
(51) Humphrey, W.; Dalke, A.; Schulten, K. VMD: Visual molecular dynamics. *J. Mol. Graph.* **1996**, *14* (October 1995), 33−38.
(52) Miles, A. J.; Wallace, B. A. Circular Dichroism Spectroscopy of Membrane Proteins. *Chem. Soc. Rev.* **2016**, *45* (18), 4859−4872.
(53) Altenbach, C.; Flitsch, S. L.; Khorana, H. G.; Hubbell, W. L. *Spin Labeling of Bacteriorhodopsin Mutants at Unique Cysteines.* **1989**, *28*, 7806−7812.
(54) Perozo, E.; Cortes, D. M.; Cuello, L. G. Three-Dimensional Architecture and Gating Mechanism of a K+ Channel Studied by EPR Spectroscopy. *Nat. Struct. Biol.* **1998**, *5* (6), 459−469.
(55) Jeschke, G.; Bender, A.; Schweikardt, T.; Panek, G.; Decker, H.; Paulsen, H. Localization of the N-Terminal Domain in Light-Harvesting Chlorophyll a/b Protein by EPR Measurements. *J. Biol. Chem.* **2005**, *280* (19), 18623−18630.
(56) Vásquez, V.; Sotomayor, M.; Marien Cortes, D.; Roux, B.; Schulten, K.; Perozo, E. Three-Dimensional Architecture of Membrane-Embedded MscS in the Closed Conformation. *J. Mol. Biol.* **2008**, *378* (1), 55−70.
(57) Mchaourab, H. S.; Kálai, T.; Hideg, K.; Hubbell, W. L. Motion of Spin-Labeled Side Chains in T4 Lysozyme: Effect of Side Chain Structure. *Biochemistry* **1999**, *38* (10), 2947−2955.
(58) Isas, J. M.; Langen, R.; Haigler, H. T.; Hubbell, W. L. Structure and Dynamics of a Helical Hairpin and Loop Region in Annexin 12: A Site-Directed Spin Labeling Study. *Biochemistry* **2002**, *41* (5), 1464−1473.
(59) Jao, C. C.; Hegde, B. G.; Gallop, J. L.; Hegde, P. B.; McMahon, H. T.; Haworth, I. S.; Langen, R. Roles of Amphipathic Helices and the Bin/Amphiphysin/Rvs (BAR) Domain of Endophilin in Membrane Curvature Generation. *J. Biol. Chem.* **2010**, *285* (26), 20164−20170.
(60) Kryshtafovych, A.; Schwede, T.; Topf, M.; Fidelis, K.; Moult, J. Critical Assessment of Methods of Protein Structure Prediction (CASP)—Round XIII. *Proteins Struct. Funct. Bioinforma.* **2019**, *87* (12), 1011−1020.
(61) Rohl, C. A.; Strauss, C. E. M.; Misura, K. M. S.; Baker, D. Protein Structure Prediction Using Rosetta. *Methods Enzymol.* **2004**, *383* (2003), 66−93.
(62) Wagner, J. R.; Sørensen, J.; Hensley, N.; Wong, C.; Zhu, C.; Perison, T.; Amaro, R. E. POVME 3.0: Software for Mapping Binding Pocket Flexibility. *J. Chem. Theory Comput.* **2017**, *13* (9), 4584−4592.
(63) Piana, S.; Lindorff-Larsen, K.; Shaw, D. E. How Robust Are Protein Folding Simulations with Respect to Force Field Parameterization? *Biophys. J.* **2011**, *100* (9), L47−L49.
(64) Allouche, A. Software News and Updates Gabedit — A Graphical User Interface for Computational Chemistry Softwares. *J. Comput. Chem.* **2011**, *32*, 174−182.
(65) Rowlett, V. W.; Mallampalli, V. K. P. S.; Karlstaedt, A.; Dowhan, W.; Taegtmeyer, H.; Margolin, W.; Vitrac, H. The Impact of Membrane Phospholipid Alterations in Escherichia Coli on Cellular Function. *J. Bacteriol.* **2017**, *199* (13), 1−22.
(66) Javadpour, M. M.; Juban, M. M.; Lo, W. C. J.; Bishop, S. M.; Alberty, J. B.; Cowell, S. M.; Becker, C. L.; McLaughlin, M. L. De Novo Antimicrobial Peptides with Low Mammalian Cell Toxicity. *J. Med. Chem.* **1996**, *39* (16), 3107−3113.
(67) Mól, A. R.; Castro, M. S.; Fontes, W. NetWheels: A Web Application to Create High Quality Peptide Helical Wheel and Net Projections. *bioRxiv* **2018**, DOI: 10.1101/416347.
(68) Gofman, Y.; Haliloglu, T.; Ben-Tal, N. The Transmembrane Helix Tilt May Be Determined by the Balance between Precession Entropy and Lipid Perturbation. *J. Chem. Theory Comput.* **2012**, *8* (8), 2896−2904.